PHYSICAL REVIEW B **112**, 205118 (2025)

Finite-temperature real-time properties of magnetic polarons in two-dimensional quantum antiferromagnets

Toni Guthardt,[1] Markus Scheb,[1] Jan von Delft,[1,2] Fabian Grusdt,[1,2] and Annabelle Bohrdt[1,2,3]
[1]*Department of Physics and Arnold Sommerfeld Center for Theoretical Physics (ASC), Ludwig-Maximilians-University Munich, Theresienstrasse 37, D-80333 Munich, Germany*
[2]*Munich Center for Quantum Science and Technology, Schellingstrasse 4, D-80799 Munich, Germany*
[3]*Institut für Theoretische Physik, Universität Regensburg, D-93035 Regensburg, Germany*

(Received 11 April 2025; revised 24 September 2025; accepted 24 September 2025; published 14 November 2025)

Due to significant progress in quantum gas microscopy in recent years, there is a rapidly growing interest in real-space properties of single mobile dopands created in correlated antiferromagnetic (AFM) Mott insulators. However, a detailed numerical description remains challenging, even for simple toy models. As a consequence, previous numerical simulations for large systems were largely limited to $T = 0$. To provide guidance for cold-atom experiments, numerical calculations at finite temperature are required. Here, we numerically study the real-time properties of a single mobile hole in the 2D t-J model at finite temperature and draw a comparison to features observed at $T = 0$. We find that a three-stage process of hole motion, which was reported at $T = 0$, is valid even at finite temperature. However, already at low temperatures, the average hole velocity at long times is not simply proportional to the spin coupling, contrary to the $T = 0$ behavior. Comparing our finite-temperature numerical results with the experimental data from quantum gas microscopy we find a qualitative disagreement: in experiment, hole spreading speeds up with increasing J/t, while in our numerics it slows down. The latter is consistent with the numerical findings previously reported at $T = 0$.

DOI: 10.1103/bm51-wq36

I. INTRODUCTION

The parent compound of cuprate superconductors is believed to be a two-dimensional Heisenberg antiferromagnet (AFM) [1]. In addition, it is generally assumed that an interplay between hole motion and antiferromagnetism is at the heart of high-temperature superconductivity in cuprates [2]. Therefore, it is of great interest to study the behavior of a single mobile charge carrier in an antiferromagnetic spin background [3–11], forming a so-called magnetic polaron.

Previous theoretical studies of the real-space motion of a hole in an AFM spin background [4,12–18] have shown that the dynamics at $T = 0$ follows a three-stage process, involving ballistic hole spreading, the emergence of a polaron, and ballistic polaron spreading. However, the behavior at finite temperature is not yet fully understood. In addition to numerical simulation [13,19–27] various semianalytical and variational approaches [28–37] have been employed to investigate polaron formation. In the conventional magnetic polaron picture, the polaron can be understood as a cloud of correlated magnons dressing the hole [12,28–30]. It has been shown that a parton picture [14,19,38,39], first suggested by Béran *et al.* [40] for describing the underlying magnetic polaron, is able to capture the relevant physics qualitatively. Here, a magnetic polaron consists of a holon, carrying the charge, which is connected by a string of displaced spins with a spinon, carrying the spin [13,14,40]. In one of the simplest approximate descriptions of a magnetic polaron in the parton picture the so-called frozen spin approximation (FSA) is used, which considers only charge fluctuations along strings of displaced spins and leaves the wave function of the surrounding spins unaffected by hole hopping [13,39,41]. In this work, we aim to test to which extent predictions of this parton model are valid at finite temperature.

In a complementary line of work, there has been significant recent progress in the study of the real-space properties of magnetic polarons experimentally using quantum gas microscopy (QGM) [42,43]. This progress has enabled the first real-space observation of magnetic polarons in equilibrium [44] and out of equilibrium [11]. By employing this technique, it is possible to perform large-scale two-dimensional simulations at finite temperature and to study both real-space and time properties. These finite-temperature simulations are a first step towards understanding the intriguing finite-temperature phases observed in cuprates. Hence, it is essential to perform numerical calculations at finite temperature in order to provide guidance for QGM.

Here, we report on the numerical simulation of the real-space, finite-temperature dynamics of a hole in a four-leg cylinder described by the t-J model, see Figs. 1(a) and 1(b). First, we observe that the main stages of hole motion reported at $T = 0$ [4,12–14,19] are valid even at finite temperature. However, contrary to the $T = 0$ behavior, the hole velocity observed for times larger than $1/J$ is not proportional to the

---

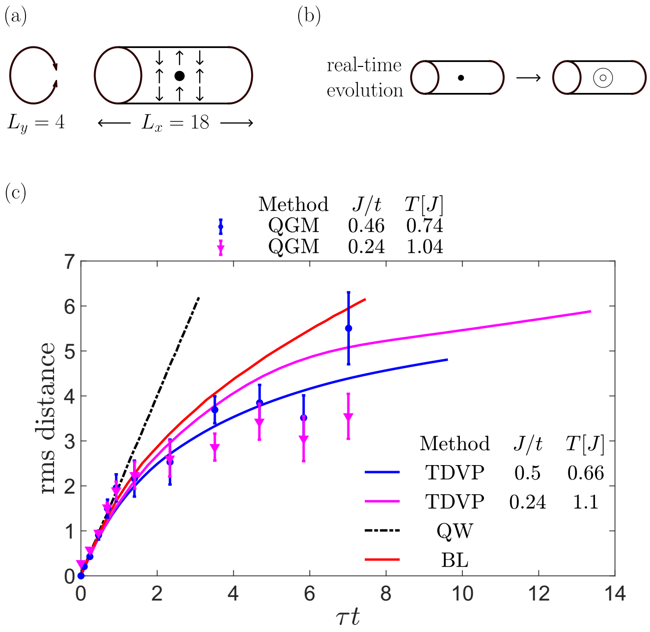

FIG. 1. (a) Illustration of the cylinder used in the simulation. The system is displayed in the configuration present at the beginning of the time evolution. The black circle represents the hole density and the arrows correspond to spin. (b) Illustration of the real-time spreading of the hole. (c) Comparison of numerical data with experimental QGM results [11]. The plot displays the root-mean-square (rms) hole distance [defined in Eq. (7)] as a function of time τ. The numerical data computed on a cylinder was extrapolated to a plain 2D lattice to allow for better comparison (see Sec. III H). The initial linear increase signifies a ballistic expansion that is consistent with a noninteracting quantum walk (QW) [11]. The subsequent slowdown of the hole can be approximated by an analytical model which is based on a free quantum walk in a Bethe lattice (BL) [11]. The data is displayed for two different J/t values.

spin coupling J. This can be seen already at temperatures $T = 0.5\,J$ and above. Second, a comparison of our numerical results with experimental data from QGM reveals short time agreement, see Fig. 1(c) (and Sec. III H for a detailed discussion). However, starting at intermediate times, we observe disagreement in the behavior of the J/t dependence of hole dynamics: in experiment, the hole spreading speeds up with increasing J/t, whereas for our numerical results it slows down. The latter is in line with the numerical behavior previously reported at $T = 0$ [4,13] and demonstrates the necessity for systematic studies and increased comparison between experiment and numerical simulation.

We would like to emphasize the nontrivial nature of our results. One might expect that thermal fluctuations at finite temperature would rapidly destroy any coherent features of the zero-temperature dynamics, especially those that rely on magnetic correlations (e.g., string formation). That the three-stage structure survives intact indicates a robustness of the magnetic polaron picture well into the finite-temperature regime. Furthermore, the universal long-time dynamics we find, depending not only on J, is a new feature that cannot be inferred from weak-coupling arguments and serves as a hallmark of the strongly correlated regime. Finally, our results provide a framework for interpreting and contrasting with recent ultracold atom experiments, offering direct experimental accessibility and testability of the features observed here.

The structure of this paper is as follows: In Sec. II, we present the numerical details of our tensor network simulation. This is followed in Sec. III by an analysis of the results of our real-time dynamics at finite temperature: We start with an introduction to the background knowledge, then illustrate the behavior of the dynamics when varying temperature and coupling ratio. This is followed by a discussion of spin correlations. Finally, we conclude this section on dynamics with a short comparison to experiment. We close in Sec. IV by discussing implications of our work and future research directions.

II. MODEL AND NUMERICS

It is generally accepted that the Fermi-Hubbard model provides a good starting point for a theoretical description of cuprates [1,45,46]. At strong coupling, it can be mapped to the t-J model up to $\mathcal{O}(t^3/U^2)$,

$$\hat{H} = -t \sum_{\langle \mathbf{ij}\rangle,\sigma} \hat{\mathcal{P}}(\hat{c}^\dagger_{\mathbf{i},\sigma}\hat{c}_{\mathbf{j},\sigma} + \text{H.c.})\hat{\mathcal{P}} + J\sum_{\langle\mathbf{ij}\rangle}\left(\hat{\mathbf{S}}_\mathbf{i}\cdot\hat{\mathbf{S}}_\mathbf{j} - \frac{\hat{n}_\mathbf{i}\hat{n}_\mathbf{j}}{4}\right), \tag{1}$$

where the first term denotes the hopping of holes with amplitude t and the second term represents the spin-exchange interactions with coupling constant $J = 4t^2/U$. Note that $\hat{\mathcal{P}}$ projects onto the space with at most one fermion per site and we neglected a three site term [47] in Eq. (1). Despite the apparent simplicity of this model, theoretical predictions and numerical simulations have proven challenging. As a consequence, previous theoretical calculations of hole dynamics have been limited to $T = 0$ behavior or required additional approximations in order to reach finite temperature [12].

All of our simulations were prepared by calculating the thermal equilibrium of the t-J model at half filling on a cylinder with length $L_x = 18$ and width $L_y = 4$, see Fig. 1(a). To that end, we used the density matrix renormalization group (DMRG) [48,49] in the language of matrix-product-states (MPSs) [50], adapted to finite temperatures via a purification scheme [51–53] and enhanced by the use of disentangling algorithms [54]. The resulting system exhibits insulating antiferromagnetic properties. We then modified it by removing a single fermion, thus enabling the subsequent motion of a hole and formation of a magnetic polaron, see Fig. 1(b). The subsequent dynamics were simulated by combining two versions of MPS-based time evolution algorithms [55]. Although the entanglement physically only spreads locally around the location of the quench, it is encoded via the virtual bonds of the MPS, which spans the entire lattice. This is why we began the time evolution with a single step of the more expensive, but global Krylov scheme [56–58]. The rest of the time evolution was performed via the local, but less expensive time-dependent-variational-principle (TDVP) algorithm [59,60]. This procedure was improved by the use of a backwards-time-evolution scheme [61–63], which allowed us to reach longer times without additional approximations. In all of the above algorithms, we also used controlled bond expansion [64,65], which effectively performs two-site optimizations at one-site costs. To guarantee the accurate implementation of the code, we conducted benchmark tests on the exactly solvable xy chain and the noninteracting tight binding chain/cylinder.

The methods described above have proven effective for extracting real-space properties of doped 2D systems. However, we note that the application of DMRG to two-dimensional systems remains a subject of active development and scrutiny. In particular, while DMRG is highly accurate and efficient for one-dimensional systems due to favorable entanglement scaling, its application to two dimensions is significantly more demanding, as the entanglement scales with the boundary length, requiring larger bond dimensions and leading to slower convergence. However, recent advancements in algorithms and computational resources, such as the use of advanced tensor network techniques like controlled bond expansion, have substantially improved both efficiency and accuracy in 2D simulations. These developments enable quantitatively reliable studies of real-space hole dynamics in 2D systems.

III. REAL TIME DYNAMICS

In this section we shed light on the real-time dynamics of a single hole at different temperatures and coupling ratios. In the following we also draw a comparison with the behavior observed at $T = 0$ and experimental results from QGM. We denote the time variable by τ, and plot it in units of either inverse tunneling $1/t$ or inverse exchange coupling $1/J$.

A. Background

Previous theoretical studies at $T = 0$ [4,12–14,19] have shown that the dynamics of a hole follows a three-stage process: (i) Initially, the hole spreads ballistically with a velocity proportional to t, independent of J, up to time $1/t$. (ii) The magnetic polaron emerges as a meson, consisting of a holon and a spinon. This process can involve damped oscillations, reflecting the structure of the meson. (iii) Starting at times $1/J$, the polaron spreads ballistically with a velocity proportional to J and independent of t.

In order to demonstrate the individual stages of the three-stage process, one can analyze the Manhattan distance r [13]

$$r = \sum_x \sum_y (|x| + |y|) \cdot n^h(x, y), \tag{2}$$

where x and y denote positions within the lattice, and $n^h(x, y)$ the corresponding hole density. The origin, with $(x, y) = (0, 0)$, is defined as the initial hole location. By examining the time-dependence of r for $T > 0$, we study how far the hole is moving from its original position. Furthermore, this allows us to gain insight into the extent to which the polaron retains its characteristics at higher temperatures.

B. Varying temperature

In Fig. 2, we compare the time evolution of the Manhattan distance $r(\tau)$ for various temperatures T, while keeping the coupling ratio t/J fixed. For all values of T and t/J, we observe the expected behavior of an initial fast spreading of the hole, followed by a slower propagation due to magnetic dressing. Note that this corresponds to a three-stage process, similar to the three stages (i–iii) reported at $T = 0$, see Sec. III A. For an analysis of the extent to which the stages (i–iii) are still present at finite temperature, see Sec. III C.

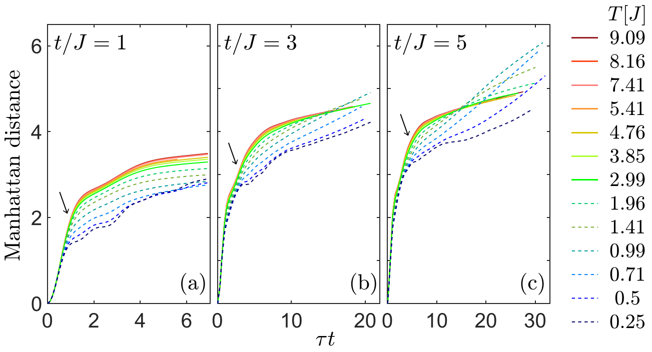

FIG. 2. Dynamics of a hole at different temperatures (colored lines) in the two-dimensional t-J model on a square lattice. The calculations are performed for $t/J = 1, 3, 5$ on a cylinder with length $L_x = 18$ and width $L_y = 4$. The plots show the Manhattan distance as a function of time τ. For all values of t/J a time of $\tau J \simeq 7$ was reached. At strong coupling, i.e., $t/J \gg 1$, and times larger than $1/J$ we observe faster spreading at low temperatures (dashed lines) than at higher temperatures (solid lines). The arrows indicate when $\tau J = 1$.

In the following, the term monotonic T-dependence is referred to as an increase/decrease of $r(\tau)$ at a fixed τ when the temperature increases/decreases. Upon closer examination, we notice that the onset of nonmonotonic T-dependence occurs at longer times τJ as t/J is decreased. For stronger coupling, $t/J > 1$, low-temperature values of r (dashed lines) stay lower for times up to $1/J$ (indicated by arrows), i.e., up to the stage of polaron formation, but start to increase more quickly at times, $\tau \approx 3/J$. As a result, $r(\tau)$ at fixed $\tau > 1/J$ is larger at intermediate temperatures than at large ones. This effect is more pronounced the higher t/J.

In the parton picture, spin-spin-correlations are necessary for a finite string tension that constrains hole expansion and binds the holon to the spinon. At short times up to $\tau \approx 1/J$ the reduction in string tension with T results in a monotonic dependence of $r(\tau)$ on T. This is due to the fact that the spinon motion can be neglected during this period. This monotonic T-dependence can be observed in Fig. 2. However, at longer times, the spinon starts to move ballistically at low temperatures. Hence, at low T, the entire magnetic polaron propagates faster. This also provides an explanation for the nonmonotonic dependence of $r(\tau)$ on T reported above.

We will further elaborate this point in the next subsection.

C. Varying the coupling ratio

In order to analyze the velocity of hole propagation, we compare the time evolution of the Manhattan distance $r(\tau)$ for three values of t/J while keeping the temperature fixed, see Fig. 3. The curves in Figs. 3(a)–3(c) and Figs. 3(d)–3(f) represent the same data, but for different scalings of the time

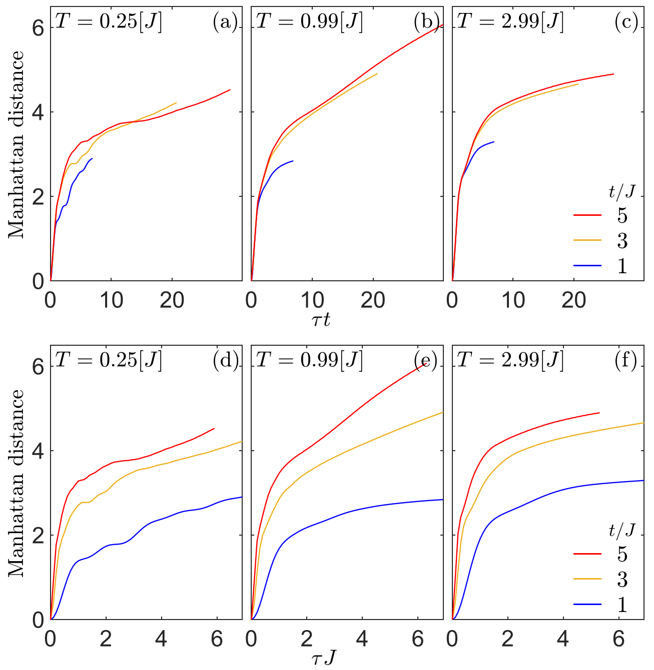

FIG. 3. Analysis of the three-stage process at finite temperature. (a)–(c) Manhattan distance is shown for three values of t/J at several temperatures as a function of time τ, plotted in units of $1/t$. (d)–(f) Analog to (a)–(c), but now plotted in units of $1/J$. The initial spreading still occurs with a velocity proportional to hopping t. For times beyond the emergence of the polaron we do only observe a simple proportionality of the expansion rate to the spin coupling J at low temperature $T = 0.25\ J$.

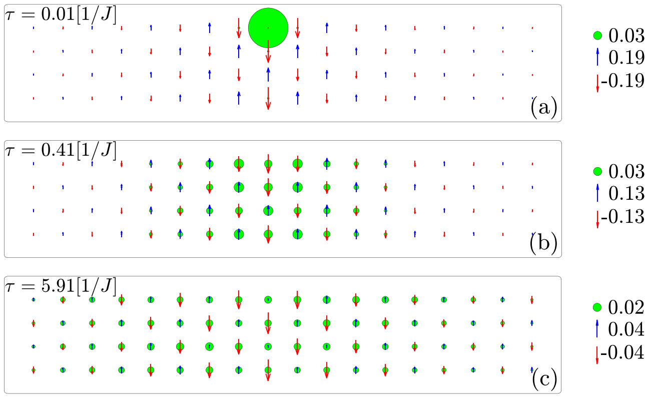

FIG. 4. Hole density and spin across the entire lattice shown for several times at temperature $T = 0.25\ J$ for $t/J = 5$. The size of the green circles represents the value of the hole density. Height and direction of the arrow correspond to absolute value and direction of spin.

axis, τt or τJ, focusing on the short- or long-time dynamics of the hole, respectively.

Figures 3(a)–3(c) reveals that the velocity initially does not depend on the spin-coupling J but only depends on hopping t, as can be seen by all curves lying on top of each other for shorter times. For all t/J values, an increase of temperature from $T = 0.25\ J$ to $T = 2.99\ J$ leads to an extension of the first stage of hole propagation. We interpret this as arising from a reduction in spin correlations, resulting in a reduction in string tension, with increasing temperature. Consequently, the time window within which the hole expansion only depends on hopping t increases. This effect is most pronounced for $t/J = 1$.

By taking a closer look at Fig. 3(d), featuring $T = 0.25\ J$, we notice that the three curves are approximately linear and parallel for larger times. Since the velocity can be estimated by dividing the Manhattan distance by time, and time is scaled in units of $1/J$, all three curves having the same slope verifies that the polaron velocity is proportional to J. However, upon increasing the temperature above $T = 0.25\ J$, the long time behavior starts to differ. For $T = 0.99\ J$, see Fig. 3(e), the different graphs, no longer run parallel to each other at large times, implying a deviation from the behavior found for the polaron model at $T = 0$. For $T = 2.99\ J$, see Fig. 3(f), the nonparallel behavior is less pronounced, but the three graphs are significantly more curved than for $T = 0.25\ J$.

Furthermore, the findings from Figs. 3(d)–3(f) are reinforced from a different perspective. By scaling time in units of $1/t$, see Figs. 3(a)–3(c), and increasing t/J, we effectively decrease J and expect a decrease of the velocity for longer times, at least for lower temperatures. This is visible in the $T = 0.25\ \ J$-plot by the crossing of the curves for $t/J = 5$ (red) and $t/J = 3$ (yellow). For $T = 0.99\ J$ and $T = 2.99\ J$, this behavior is absent, pointing again to a different behavior of polarons at longer times.

D. Hole density and spin across system

Thus far, our analysis has been limited to average distances. We now turn to site-resolved densities, which are directly accessible in quantum gas microscopes. In the following, we illustrate how both the hole density and spin evolve as a function of the lattice sites and as a function of time for a specific temperature $T = 0.25\ J$ with $t/J = 5$, see Fig. 4. At this point it is also important to mention that initially, an electron with spin down was removed from the equilibrium system, resulting in a total spin $S_z^{\text{tot}} \neq 0$.

In Fig. 4(a) we observe how the short-time symmetric spreading of the hole, starting at the initial hole position, results in spins being aligned in the same direction at sites adjacent to the initial hole position. This observation reflects that $S_z^{\text{tot}} \neq 0$. The initial hole position is located in the center of the cylinder and corresponds to the site with the largest hole density present at such short times. This indicates that the hole is still mainly located at the initial site.

At intermediate times, see Fig. 4(b), the hole has already spread over one third of the length of the cylinder. In the process of spreading it has distorted the spin order around the initial hole position significantly more compared to Fig. 4(a). It is important to point out that the parallel alignment of spins found at the initial hole location is characteristic of a spinon. Note, however, that the identification of a spinon in a rigorous sense would require more direct evidence. The observed spin configurations indicate localized spin distortions trailing the hole. Such features are often associated with spinon-like behavior in the context of magnetic polarons.

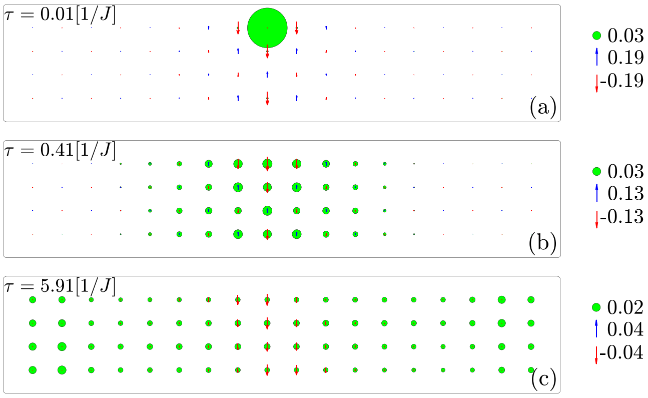

FIG. 5. Same as Fig. 4, but for $T = 0.99\,J$ and $t/J = 5$.

Displacing spins in an AFM background comes at an energy cost. This slows the initial fast spreading of the hole at times $1/t$, which we observe here.

Finally at long times, see Fig. 4(c), we can see the reemergence of AFM correlations in the whole system and an almost uniform distribution of the hole density over the entire lattice, indicating the return of the system into equilibrium. However, it should be noted that true equilibrium has not yet been reached at this point. In addition, the observed staggered spin structure is a local feature and does not imply long-range order or spontaneous symmetry breaking.

In combination, Fig. 4 is a direct demonstration of the three-stage process in real-space, (i) starting with the fast hole spreading in Fig. 4(a), (ii) followed by the magnetic polaron formation in Fig. 4(b), and (iii) concluding with the spinon spreading in Fig. 4(c).

Figure 5 presents analogous results at a higher temperature $T = 0.99[J]$. One observes a similar behavior compared to Fig. 4, but the hole motion generally takes place faster and the average spin expectation value is reduced significantly. Nevertheless, the spatial heterogeneity of the hole density at long times indicates that the system has not yet reached a state of near-equilibrium, see Fig. 5(c). This phenomenon may be attributed to finite size effects. At the same point in time one also observes a slight asymmetry in the spin data with respect to mirroring the data along the initial hole position. This presumably is due to accumulation of errors in the numerical simulation, which affect the rather small spins at such temperatures more severely. Furthermore, we can see that no AFM spin patterns have built up at our longest time.

E. Next-nearest-neighbor spin correlations

The process of polaron creation and subsequent polaron spreading can also be analyzed by considering the evolution of spin correlations. In equilibrium, i.e., directly before we remove an electron from our system and study its dynamics, we can observe non-negligible local AFM correlations for temperatures $T \lesssim 1J$, see Appendix A.

To gain further insights into the evolution of spin correlations, we study staggered spin correlations, which are evaluated between sites $\mathbf{r}$ and $\mathbf{r}'$ and defined as

$$C_{\mathbf{r}}(\mathbf{d}) = (-1)^{d_x+d_y} 4\big(\langle \hat{S}^z_{\mathbf{r}} \hat{S}^z_{\mathbf{r}+\mathbf{d}} \rangle - \langle \hat{S}^z_{\mathbf{r}} \rangle \langle \hat{S}^z_{\mathbf{r}+\mathbf{d}} \rangle\big). \tag{3}$$

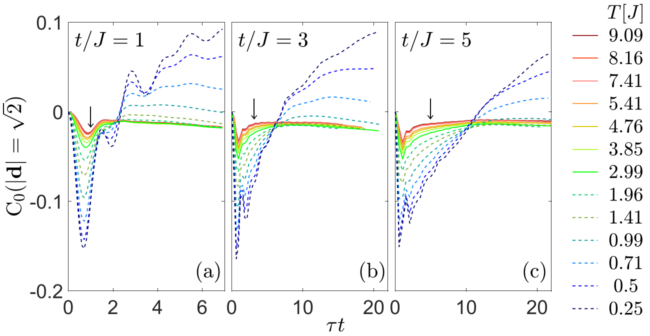

FIG. 6. Staggered next nearest-neighbor spin correlations between the initial hole position and its diagonal neighbors as function of time. Data is displayed for several t/J at different temperatures. The arrows indicate when $\tau J = 1$.

Here, $\mathbf{d}$ is defined as the difference vector between respective sites $\mathbf{r}$ and $\mathbf{r}'$ and $\hat{S}^z$ is defined as the usual z component of the spin operator $\hat{\mathbf{S}}$. Note that as a consequence of this definition, positive correlation values correspond to AFM correlations.

We start by considering the corresponding next-nearest-neighbor correlations $C_0(|\mathbf{d}| = \sqrt{2})$. In Fig. 6 we display the staggered next-nearest-neighbor spin correlation (SNNNC) as a function of time and relative to the initial hole position. This has been a common choice in experiment [11], facilitating comparisons. The correlations are evaluated for different temperatures at three values of t/J.

We observe for all values of t/J at all temperatures that the system is out of equilibrium during short and intermediate times, testified by the presence of negative correlation values, and only slowly approaches a steady state for long times. For times up to $1/t$, $C_0(|\boldsymbol{d}| = \sqrt{2})$ is negative and increases even further in magnitude. This is connected to the fast initial spreading of the hole with a velocity proportional to t. When the hole performs one hop, it places the neighboring spin on the "origin". As a result, the spin is situated in the "wrong" sublattice, leading to negative $d = \sqrt{2}$ spin correlations. During the phase of polaron emergence, which occurs for times $1/t < \tau < 1/J$, the SNNNC approaches zero quickly and only slows down when the polaron is fully formed. At times larger than $1/J$, when the polaron is moving as a whole, the SNNNC continues to relax to equilibrium, but slower compared to the stage of polaron emergence. Given that the polaron is moving as a whole, the relaxation to equilibrium can also be understood as a consequence of spinon motion away from the origin.

Furthermore we can see that at $T < 2\,J$ (dashed lines) the negative correlations relax to zero much faster for strong spin coupling, i.e., small t/J. This phenomenon can be attributed to the relaxation of spin correlation at the origin, which is a consequence of the motion of the spinon away from the origin. Given that spinon motion occurs on time scales of $1/J$, the findings presented on time scales of $1/t$, see Fig. 6, can be explained.

Since in equilibrium a finite string length of the polaron requires finite spin correlations [13,14,39], it is also of interest to determine the temperature up to which finite spin correlations are visible. This should indicate the transition to a

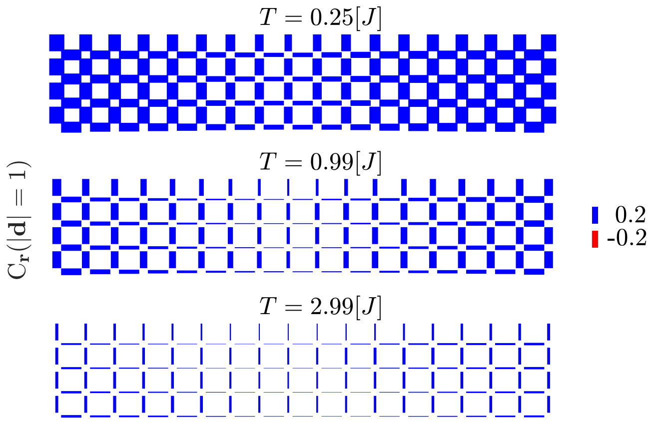

FIG. 7. Staggered nearest-neighbor (SNNC) spin correlations in the entire lattice for $t/J = 5$. Data is plotted at different temperatures at the maximum calculated time $\tau = 6/J$. The bars represent the SNNC spin correlations connecting neighboring sites. The thickness and the color of the bars represents the absolute value and the sign of the spin correlation.

region where no polarons emerge. We find an absence of spin correlations close to the origin at all times for temperatures above $T \approx 2\,J$, with nonvanishing positive spin correlations only present at long times for temperatures smaller $T \approx 1\;\;J$. This temperature scale is in line with the temperature at which one would expect to see a return of AFM correlations due to a competition between temperature and spin coupling. In addition, the complete lack of spin correlations for temperatures above $T = 2\,J$ also suggests that magnetic polarons do not survive in that temperature range.

F. Nearest-neighbor-spin correlations

To further improve our intuitive understanding, we now build on the scenario described in Sec. III D by discussing the distribution of spin correlations over the entire lattice as a function of temperature.

To this end, we take a closer look at the staggered nearest-neighbor (SNNC) spin correlations, see Fig. 7. Here, we present the distribution of the spin correlations over the entire lattice for $t/J = 5$ at the maximal reached time $\tau = 6/J$. By examining the long-term correlations, we aim to determine whether we can identify features that are characteristic of a system close to equilibrium, such as a homogeneous spin correlation, or alternatively, whether we can observe features that must be explained due to the dynamics of the doped system.

Overall, we observe that the average strength of the spin correlation reduces with increasing temperature, as expected. Since these data show that spin correlations have become very weak for temperatures above $T = 0.99\,J$, they support the observations of Sec. III E.

Furthermore, we see a relatively uniform distribution of spin correlation, only the spin correlations around the initial hole position have not yet reached equilibrium. This leads to the conclusion that the system is approaching equilibrium at the end of the time evolution, in agreement with Sec. III D.

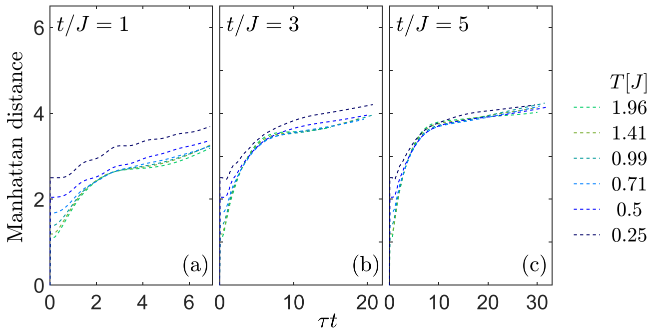

FIG. 8. Manhattan distance of the spinon. The spinon density used here is defined as the normalized deviation of the SNNC from its equilibrium value. The data is displayed for several t/J and different temperatures, up to which polarons are expected to exist.

G. Spinon spreading

To conclude the discussion of the temperature dependence, we shed light on the spinon spreading. In order to achieve this, we define the spinon density $n^s(x, y)$ as the normalized deviation of the SNNC from its equilibrium value,

$$n^s(x, y) = \sum_{|\boldsymbol{d}|=1} \left|C_{(x,y)}(\boldsymbol{d}) - C^{\text{equil}}_{(x,y)}(\boldsymbol{d})\right|/h, \tag{4}$$

with $h = \sum_{x,y}\sum_{|\boldsymbol{d}|=1}(|C_{(x,y)}(\boldsymbol{d}) - C^{\text{equil}}_{(x,y)}(\boldsymbol{d})|)$ being the normalization factor. It is crucial to acknowledge that this definition is only valid in the context of temperatures where polarons exist. Figure 8 illustrates the Manhattan distance r_s of the spinon for varying values of t/J and temperatures. In analogy to the Manhattan distance r defined for the hole, the Manhattan distance r_s of the spinon is defined as

$$r_s = \sum_x \sum_y (|x| + |y|) \cdot n^s(x, y). \tag{5}$$

Overall, the data indicate that the spinon spreading also follows a three-stage process, similar to the spreading of the hole.

Within a single short time step $\delta\tau = 0.01/J$, a pronounced increase in the spinon distance, r_s, is observed, with the greatest increase occurring at low temperatures. This can be attributed to the presence of AFM correlations in equilibrium at low temperatures. The removal of an electron and subsequent hopping of the hole for a short time step results in the emergence of ferromagnetic correlations adjacent to the initial hole position. This corresponds to a significant deviation from the equilibrium correlations, which is reflected in a steep increase in the spinon distance r_s.

Following the initial time step, the velocity of spinon spreading is observed to increase with temperature. This behavior persists up to medium times and is especially pronounced in the case of $t/J > 1$. It is noteworthy that this behavior is consistent with the behavior of the hole, which also features an increase in spreading velocity with temperature in the case of $T < 2\,J$ and similar times, see Sec. III B.

At long times, $\tau > 1/J$, the velocity of spinon spreading is observed to be similar for different temperatures. However, the absolute spinon distance r_s reached at long times is slightly higher for lower temperatures. This is in contrast to the long-time spreading of the hole, see Sec. III B, which reaches further distances the higher the temperature in the case of $T < 1J$ at strong coupling. It is likely that this discrepancy can be attributed to a reduction in the binding strength between the holon and the spinon as the temperature increases, which in turn permits a further propagation of the hole.

H. Comparison with experiment

To conclude with the discussion of the hole dynamics we draw a comparison with experimental results using QGM [11]. To this end, we calculate the root-mean-square (rms) hole distance

$$d_{\mathrm{rms}} = \sqrt{\sum_x \sum_y (|x|^2 + |y|^2) \cdot n^h(x, y)}, \tag{6}$$

where x and y denote positions within the lattice, and $n^h(x, y)$ the corresponding hole density. Analogous to the definition of the Manhattan distance, the origin is defined as the initial hole location. Note that we used $\sum_x \sum_y n^h(x, y) = 1$.

The results are presented in Fig. 1(c) of the introduction. There, we compare the rms distance obtained using our numerics on a cylinder with results from QGM for a plain 2D lattice. Note that the experimental QGM data has been generated for the Hubbard model, whereas our numerical data was computed for the t-J model. For better comparison, our numerical results computed on a cylinder were extrapolated to a plain 2D lattice by assuming equivalent long-time expansion in x and y directions

$$d_{\mathrm{rms}} = \sqrt{\langle x^2\rangle + \langle y^2\rangle} \approx \sqrt{2}\sqrt{\langle x^2\rangle}, \tag{7}$$

with $\langle x\rangle = \sum_x x \cdot n^h(x)$. The results are displayed for two different J/t values at similar temperatures. For short times up to $\tau \approx 1/t$ we observe good agreement between experiment and numerical simulation. However, starting at intermediate times we find that the J/t-dependence observed numerically is contrary to the J/t-dependence obtained in experiment: In experiment, the hole spreading speeds up with increasing J/t (blue lines lie lower than red lines), whereas for the numerical results it slows down (blue symbols lie higher than red symbols). Since the numerically observed behavior is in line with previous numerical study at $T = 0$ [4,13], further analysis is needed to reconcile the experimental measurements with numerical results.

IV. SUMMARY AND OUTLOOK

In this work, we numerically studied the real-time dynamics of a single hole in the 2D t-J model at finite temperature.

We observed that a three-stage process of hole motion previously observed for $T = 0$ is valid even at finite temperature. In the strong coupling limit, i.e., $t/J \gg 1$, we observe that the speed of hole spreading decreases with temperature at long times. This suggests strong scattering on thermal excitations, which is not included in the parton model that we use to explain the qualitative behavior at low temperatures. Furthermore, our data shows that the long time spreading is not solely dependent on the spin coupling J, indicating that spinons and chargons are no longer bound at high temperatures.

Furthermore, our findings reveal that, at finite temperature, the initial stage of hole motion is solely dependent on the hopping t. Moreover, for all values of t/J, an increase in T results in the prolongation of the initial stage of hole motion.

Additionally, the comparison of our numerical results with experimental data from QGM reveals that the hole spreading speeds up with increasing J/t starting at intermediate times, whereas for our numerical results it slows down. In view of the fact that our findings are in accordance with those of previous numerical analysis performed at $T = 0$ in the t-J model, we attribute this discrepancy to shortcomings in the theoretical modeling of the experimental setup. It will consequently be intriguing to see whether subsequent studies with QGM can resolve this discrepancy.

The nontrivial nature of our findings deserves emphasis. Thermal fluctuations at finite temperature might be expected to quickly wash out coherent features of the zero-temperature dynamics—particularly those tied to magnetic correlations, such as string formation. The fact that the three-stage structure remains clearly visible highlights the remarkable robustness of the magnetic polaron picture in the finite-temperature regime. In addition, the breakdown of the linear relationship between long-time hole velocity and J marks a qualitatively new feature that cannot be anticipated from weak-coupling arguments and is characteristic of strong correlations. Finally, our results provide a concrete framework for interpreting and benchmarking with recent ultracold atom experiments, offering direct experimental access to the finite-temperature dynamics explored here.

Another highly interesting direction for future research would be the investigation of finite doping, e.g., the case of two holes. At $T = 0$, both a highly mobile bound pair with a dispersion proportional to t and a heavy pair, which moves due to spin exchange processes, have been found [66]. It will be exciting to see whether similar features can be confirmed at finite temperature and to enhance our understanding of the pairing mechanism in cuprates.

While our analysis has focused on intuitive and experimentally accessible observables—such as the average Manhattan distance and real-space snapshots—to reveal the dynamical regimes of magnetic polarons, the full access to the many-body wave function also allows for the extraction of more intrinsically quantum information. For instance, string-length distributions or the entanglement entropy between the hole and the spin background could provide deeper insight into the quantum nature of polaron formation. We identify these and related observables as promising directions for future theoretical and experimental exploration.

Since our numerical data can be compared directly to QGM data, our research offers guidance for ultracold atom experiments. These experiments have the capability of studying individual magnetic polarons at finite temperature in both real and frequency space. It will therefore be fascinating to see whether a systematic experimental study of the temperature dependence will shed additional light on finite-size effects or the equilibration dynamics at even longer times.

Here we have discussed the finite-temperature real-time properties of magnetic polarons. In a follow-up paper [67] we present our results for the one-hole spectral function in a t-J model at finite temperature, providing a complementary perspective on the frequency and momentum characteristics of magnetic polarons. While the present work focuses on the real

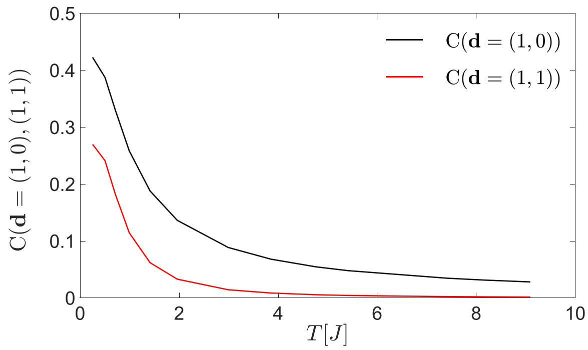

FIG. 9. Staggered spin correlations $C_{\mathbf{r}}(\mathbf{d})$ [Eq. (3)] in equilibrium as a function of temperature. The data presented here was computed on the same t-J cylinder as that discussed in the main text and shows nearest (black) and next-nearest-neighbor (red) correlations.

space dynamics of hole motion, which is particularly relevant for quantum gas microscopy, the follow-up study concentrates on spectral features and their temperature dependence, which is particularly relevant for photoemission experiments.

ACKNOWLEDGMENTS

We thank Sebastian Paeckel for helpful discussions. Symmetries in tensor network computations were exploited using the QSpace tensor library [68–70]. This work was funded in part by the Deutsche Forschungsgemeinschaft under Germany's Excellence Strategy EXC-2111 (Project No. 390814868). It is part of the Munich Quantum Valley, supported by the Bavarian state government with funds from the Hightech Agenda Bayern Plus. F.G. acknowledges funding from the European Research Council (ERC) under the European Union's Horizon 2020 research and innovation programm (Grant Agreement No. 948141)—ERC Starting Grant SimUcQuam.

DATA AVAILABILITY

The data that support the findings of this article are not publicly available upon publication because it is not technically feasible and/or the cost of preparing, depositing, and hosting the data would be prohibitive within the terms of this research project. The data are available from the authors upon reasonable request.

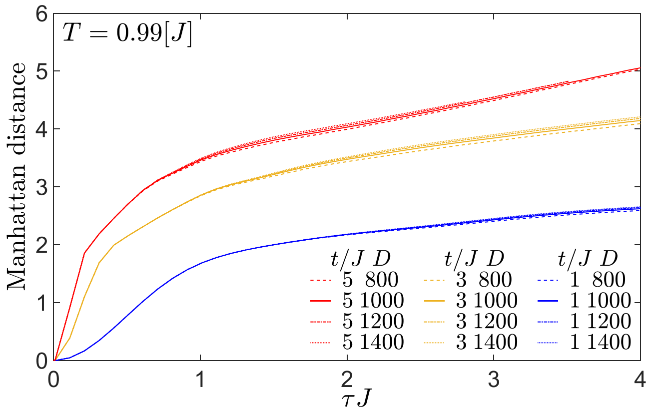

FIG. 10. Convergence with bond dimension D in the Manhattan distance at $T = 0.99\,J$ for $t/J = 1, 3, 5$.

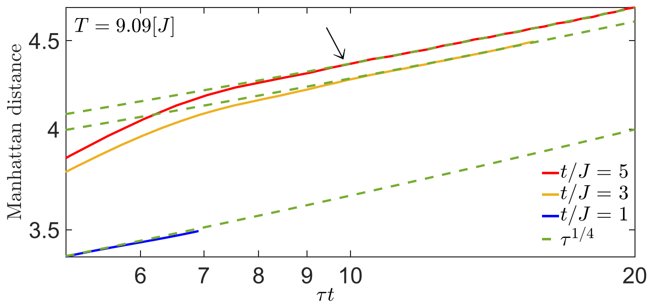

FIG. 11. Analysis of the high temperature dynamics. Logarithmic plot of the Manhattan distance for different t/J as function of time. The data is plotted against a subdiffusive process (green dashed line), which has been shifted to coincide with the beginning of the respective long-term dynamics. The black arrow indicates the point in time at which the hole has reached the edge of the cylinder.

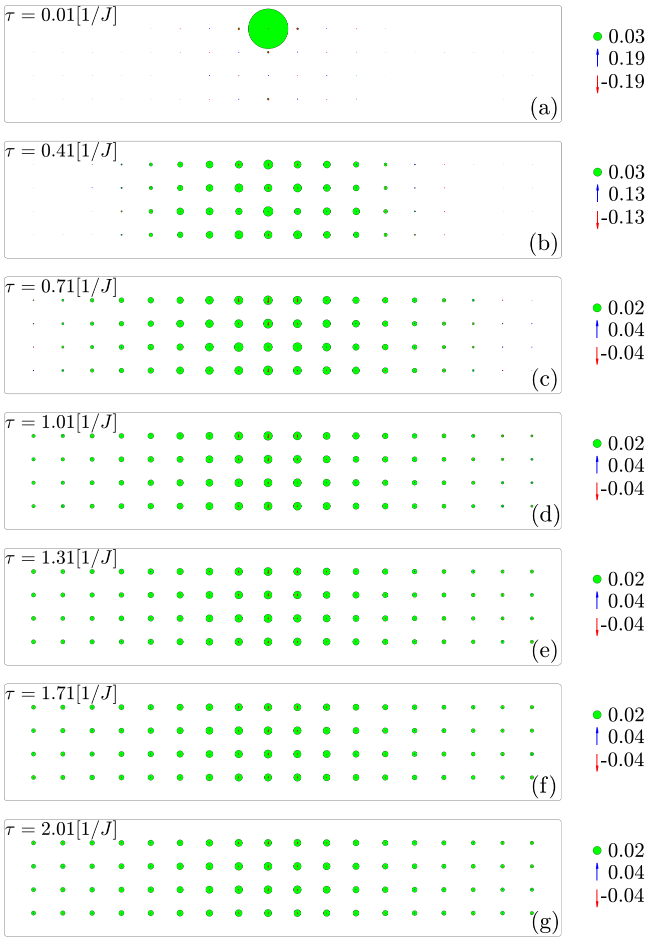

FIG. 12. Hole density and spin across the entire lattice shown for several times at temperature $T = 9.09\,J$ for $t/J = 5$. The data is displayed in the same way as Fig. 4.

APPENDIX A: SPIN CORRELATIONS IN EQUILIBRIUM

Given that spin correlations are required for the existence of a finite string tension, it is instructive to observe the presence of spin correlations in equilibrium. In Fig. 9 we present the evolution of nearest and next-nearest-neighbor spin correlations in equilibrium as a function of temperature.

APPENDIX B: CONVERGENCE

The results presented in the main text have been subjected to meticulous analysis with regard to convergence in a number of parameters, including the bond dimension D, see Fig. 10 for an exemplary analysis.

APPENDIX C: HOLE SPREADING AT HIGH TEMPERATURE

By approximating the hole motion at infinite temperature as a diffusive quantum random walk on the Bethe lattice with a disorder potential [3,13], it was shown that the long-term propagation of the hole in the t-J_z model is subdiffusive when considering the case of infinite temperature and large J_z/t. Although our calculations are limited to a finite system size, making it difficult to observe diffusion processes, we have analyzed whether similar subdiffusive behavior can be observed for the more challenging t-J model.

In Fig. 11 we compare the intermediate to long-time Manhattan distance for our highest temperature $T = 9.09J$ against the $\tau^{1/4}$ behavior (dashed lines) expected for the subdiffusive expansion in the Bethe-lattice model. By scaling the time in units of $1/t$ and displaying the behavior for different values of t/J, we effectively show how the spin coupling J affects the high temperature dynamics. For small spin couplings, i.e., $t/J \gg 1$ (red line), we find remarkably good agreement with the subdiffusion process displayed here. It is also worth mentioning that the type of subdiffusion observed here is identical to the subdiffusion previously reported for the t-J_z model.

This subdiffusive behavior can also be understood in terms of a disorder potential on a Bethe lattice, which slows down the hole expansion. As a result of spin couplings, the movement of the hole from one site to another modifies the energy of the spin system, effectively creating the aforementioned disorder potential.

Furthermore, it is important to determine the temperature at which the subdiffusion behavior ceases to exist. As the long-time behavior for $T \geqslant 2.99$ remains essentially independent of temperature in the case of $t/J \gg 1$, see solid lines in Fig. 2, we conclude that for small spin couplings, i.e., $t/J \gg 1$, this subdiffusive behavior persists down to a temperature of $T \approx 2\,J$.

In order to asses to which extent diffusion can be observed in our finite-size cylinder we extract the point in time at which the hole reaches the left and right edges of the cylinder, see Fig. 12. If the hole density at all edge sites is above a threshold value n^h_{tresh}, we assume that the hole has reached the left and right edges of the cylinder. We set the threshold value to $n^{\text{h}}_{\text{tresh}} = 0.01$. At $t/J = 5$ and $T = 9.09\,J$ we find that the hole reaches the left and right edges of the cylinder at time $\tau \approx 2[1/J]$, which corresponds to the time up to which diffusion can be observed in the system.

---

[1] P. A. Lee, N. Nagaosa, and X.-G. Wen, Doping a Mott insulator: Physics of high-temperature superconductivity, Rev. Mod. Phys. **78**, 17 (2006).

[2] C. Proust and L. Taillefer, The remarkable underlying ground states of cuprate superconductors, Annu. Rev. Condens. Matter Phys. **10**, 409 (2019).

[3] M. Kanász-Nagy, I. Lovas, F. Grusdt, D. Greif, M. Greiner, and E. A. Demler, Quantum correlations at infinite temperature: The dynamical Nagaoka effect, Phys. Rev. B **96**, 014303 (2017).

[4] K. K. Nielsen, T. Pohl, and G. Bruun, Nonequilibrium hole dynamics in antiferromagnets: damped strings and polarons, Phys. Rev. Lett. **129**, 246601 (2022).

[5] K. Nielsen, M. Bastarrachea-Magnani, T. Pohl, and G. Bruun, Spatial structure of magnetic polarons in strongly interacting antiferromagnets, Phys. Rev. B **104**, 155136 (2021).

[6] J. Vijayan, P. Sompet, G. Salomon, J. Koepsell, S. Hirthe, A. Bohrdt, F. Grusdt, I. Bloch, and C. Gross, Time-resolved observation of spin-charge deconfinement in fermionic Hubbard chains, Science **367**, 186 (2020).

[7] K. Kurokawa, S. Isono, Y. Kohama, S. Kunisada, S. Sakai, R. Sekine, M. Okubo, M. D. Watson, T. K. Kim, C. Cacho *et al.*, Unveiling phase diagram of the lightly doped high-T_c cuprate superconductors with disorder removed, Nat. Commun. **14**, 4064 (2023).

[8] M. Qiao, G. Emperauger, C. Chen, L. Homeier, S. Hollerith, G. Bornet, R. Martin, B. Gély, L. Klein, D. Barredo *et al.*, Realization of a doped quantum antiferromagnet with dipolar tunnelings in a Rydberg tweezer array, Nature (London) **644**, 889 (2025).

[9] A. Bohrdt, D. Wei, D. Adler, K. Srakaew, S. Agrawal, P. Weckesser, I. Bloch, F. Grusdt, and J. Zeiher, Microscopy of bosonic charge carriers in staggered magnetic fields, arXiv:2410.19500.

[10] L. Hahn, A. Bohrdt, and F. Grusdt, Dynamical signatures of thermal spin-charge deconfinement in the doped Ising model, Phys. Rev. B **105**, L241113 (2022).

[11] G. Ji, M. Xu, L. H. Kendrick, C. S. Chiu, J. C. Brüggenjürgen, D. Greif, A. Bohrdt, F. Grusdt, E. Demler, M. Lebrat, and M. Greiner, Coupling a mobile hole to an antiferromagnetic spin background: Transient dynamics of a magnetic polaron, Phys. Rev. X **11**, 021022 (2021).

[12] K. Shen, K. Sun, M. F. Gelin, and Y. Zhao, Finite-temperature hole–magnon dynamics in an antiferromagnet, J. Phys. Chem. Lett. **15**, 447 (2024).

[13] A. Bohrdt, F. Grusdt, and M. Knap, Dynamical formation of a magnetic polaron in a two-dimensional quantum antiferromagnet, New J. Phys. **22**, 123023 (2020).

[14] F. Grusdt, M. Kánasz-Nagy, A. Bohrdt, C. S. Chiu, G. Ji, M. Greiner, D. Greif, and E. Demler, Parton theory of magnetic polarons: Mesonic resonances and signatures in dynamics, Phys. Rev. X **8**, 011046 (2018).

[15] Z. Su, Y. Li, W. Lai, and L. Yu, Self-consistent renormalized hole motion in a quantum antiferromagnet, Phys. Rev. Lett. **63**, 1318 (1989).

[16] S. A. Trugman, Interaction of holes in a Hubbard antiferromagnet and high-temperature superconductivity, Phys. Rev. B **37**, 1597 (1988).

[17] P. Béran, Dynamics of a single hole in the two-dimensional *t-J* model in the presence of a magnetic field and the composite nature of quasiparticles, Phys. Rev. B **54**, 1391 (1996).

[18] A. Ramšak and P. Horsch, Spatial structure of spin polarons in the *t-J* model, Phys. Rev. B **57**, 4308 (1998).

[19] A. Bohrdt, E. Demler, F. Pollmann, M. Knap, and F. Grusdt, Parton theory of angle-resolved photoemission spectroscopy spectra in antiferromagnetic Mott insulators, Phys. Rev. B **102**, 035139 (2020).

[20] V. Elser, D. A. Huse, B. I. Shraiman, and E. D. Siggia, Ground state of a mobile vacancy in a quantum antiferromagnet: Small-cluster study, Phys. Rev. B **41**, 6715 (1990).

[21] E. Dagotto, R. Joynt, A. Moreo, S. Bacci, and E. Gagliano, Strongly correlated electronic systems with one hole: Dynamical properties, Phys. Rev. B **41**, 9049 (1990).

[22] P. W. Leung and R. J. Gooding, Dynamical properties of the single-hole *t-J* model on a 32-site square lattice, Phys. Rev. B **52**, R15711 (1995).

[23] M. Brunner, F. F. Assaad, and A. Muramatsu, Single-hole dynamics in the *t-J* model on a square lattice, Phys. Rev. B **62**, 15480 (2000).

[24] A. Mishchenko, N. Prokof'ev, and B. Svistunov, Single-hole spectral function and spin-charge separation in the *t-J* model, Phys. Rev. B **64**, 033101 (2001).

[25] S. R. White and I. Affleck, Density matrix renormalization group analysis of the Nagaoka polaron in the two-dimensional *t-J* model, Phys. Rev. B **64**, 024411 (2001).

[26] G. Sangiovanni, A. Toschi, E. Koch, K. Held, M. Capone, C. Castellani, O. Gunnarsson, S.-K. Mo, J. Allen, H.-D. Kim *et al.*, Static versus dynamical mean-field theory of Mott antiferromagnets, Phys. Rev. B **73**, 205121 (2006).

[27] F. Mezzacapo, Variational study of a mobile hole in a two-dimensional quantum antiferromagnet using entangled-plaquette states, Phys. Rev. B **83**, 115111 (2011).

[28] C. Kane, P. Lee, and N. Read, Motion of a single hole in a quantum antiferromagnet, Phys. Rev. B **39**, 6880 (1989).

[29] S. Sachdev, Hole motion in a quantum Néel state, Phys. Rev. B **39**, 12232 (1989).

[30] P. Bermes, A. Bohrdt, and F. Grusdt, Magnetic polarons beyond linear spin-wave theory: Mesons dressed by magnons, Phys. Rev. B **109**, 205104 (2024).

[31] S. Schmitt-Rink, C. Varma, and A. Ruckenstein, Spectral function of holes in a quantum antiferromagnet, Phys. Rev. Lett. **60**, 2793 (1988).

[32] G. Martinez and P. Horsch, Spin polarons in the *t-J* model, Phys. Rev. B **44**, 317 (1991).

[33] A. Auerbach and B. E. Larson, Small-polaron theory of doped antiferromagnets, Phys. Rev. Lett. **66**, 2262 (1991).

[34] Z. Liu and E. Manousakis, Dynamical properties of a hole in a Heisenberg antiferromagnet, Phys. Rev. B **45**, 2425 (1992).

[35] M. Boninsegni and E. Manousakis, Green's-function Monte Carlo study of the *t-J* model, Phys. Rev. B **46**, 560 (1992).

[36] M. Boninsegni and E. Manousakis, Variational description of a quasihole excitation in a quantum antiferromagnet, Phys. Rev. B **45**, 4877 (1992).

[37] O. A. Starykh, O. F. de Alcantara Bonfim, and G. F. Reiter, Self-consistent born approximation for the hole motion in the three-band model: a comparison with photoemission experiments, Phys. Rev. B **52**, 12534 (1995).

[38] E. Manousakis, String excitations of a hole in a quantum antiferromagnet and photoelectron spectroscopy, Phys. Rev. B **75**, 035106 (2007).

[39] F. Grusdt, A. Bohrdt, and E. Demler, Microscopic spinon-chargon theory of magnetic polarons in the *t-J* model, Phys. Rev. B **99**, 224422 (2019).

[40] P. Béran, D. Poilblanc, and R. Laughlin, Evidence for composite nature of quasiparticles in the 2D *t-J* model, Nucl. Phys. B **473**, 707 (1996).

[41] F. Grusdt, Z. Zhu, T. Shi, and E. Demler, Meson formation in mixed-dimensional *t-J* models, SciPost Phys. **5**, 057 (2018).

[42] A. Bohrdt, L. Homeier, C. Reinmoser, E. Demler, and F. Grusdt, Exploration of doped quantum magnets with ultracold atoms, Ann. Phys. **435**, 168651 (2021).

[43] C. Gross and I. Bloch, Quantum simulations with ultracold atoms in optical lattices, Science **357**, 995 (2017).

[44] J. Koepsell, J. Vijayan, P. Sompet, F. Grusdt, T. A. Hilker, E. Demler, G. Salomon, I. Bloch, and C. Gross, Imaging magnetic polarons in the doped Fermi–Hubbard model, Nature (London) **572**, 358 (2019).

[45] V. Emery, Theory of high-T_c superconductivity in oxides, Phys. Rev. Lett. **58**, 2794 (1987).

[46] E. Dagotto, Correlated electrons in high-temperature superconductors, Rev. Mod. Phys. **66**, 763 (1994).

[47] J. Spalek, *t-J* model then and now: a personal perspective from the pioneering times, arXiv:0706.4236.

[48] S. R. White, Density matrix formulation for quantum renormalization groups, Phys. Rev. Lett. **69**, 2863 (1992).

[49] S. R. White, Density-matrix algorithms for quantum renormalization groups, Phys. Rev. B **48**, 10345 (1993).

[50] U. Schollwöck, The density-matrix renormalization group in the age of matrix product states, Ann. Phys. **326**, 96 (2011).

[51] A. Nocera and G. Alvarez, Symmetry-conserving purification of quantum states within the density matrix renormalization group, Phys. Rev. B **93**, 045137 (2016).

[52] A. E. Feiguin and S. R. White, Finite-temperature density matrix renormalization using an enlarged Hilbert space, Phys. Rev. B **72**, 220401 (2005).

[53] A. E. Feiguin and G. A. Fiete, Spectral properties of a spin-incoherent Luttinger liquid, Phys. Rev. B **81**, 075108 (2010).

[54] J. M. Hauschild, Quantum many-body systems far out of equilibrium—simulations with tensor networks, Ph.D. thesis, Technische Universität München, 2019.

[55] S. Paeckel, T. Köhler, A. Swoboda, S. R. Manmana, U. Schollwöck, and C. Hubig, Time-evolution methods for matrix-product states, Ann. Phys. **411**, 167998 (2019).

[56] J. J. García-Ripoll, Time evolution of matrix product states, New J. Phys. **8**, 305 (2006).

[57] P. E. Dargel, A. Wöllert, A. Honecker, I. P. McCulloch, U. Schollwöck, and T. Pruschke, Lanczos algorithm with matrix product states for dynamical correlation functions, Phys. Rev. B **85**, 205119 (2012).

[58] M. L. Wall, Out-of-equilibrium dynamics with matrix product states, *Quantum Many-Body Physics of Ultracold Molecules in Optical Lattices* (Springer, Cham, Switzerland, 2015), pp. 177–222.

[59] J. Haegeman, J. I. Cirac, T. J. Osborne, I. Pižorn, H. Verschelde, and F. Verstraete, Time-dependent variational principle for quantum lattices, Phys. Rev. Lett. **107**, 070601 (2011).

[60] J. Haegeman, C. Lubich, I. Oseledets, B. Vandereycken, and F. Verstraete, Unifying time evolution and optimization with matrix product states, Phys. Rev. B **94**, 165116 (2016).

[61] C. Karrasch, J. H. Bardarson, and J. E. Moore, Finite-temperature dynamical density matrix renormalization group and the Drude weight of spin-1/2 chains, Phys. Rev. Lett. **108**, 227206 (2012).

[62] D. Kennes and C. Karrasch, Extending the range of real time density matrix renormalization group simulations, Comput. Phys. Commun. **200**, 37 (2016).

[63] C. Karrasch, J. Bardarson, and J. Moore, Reducing the numerical effort of finite-temperature density matrix renormalization group calculations, New J. Phys. **15**, 083031 (2013).

[64] A. Gleis, J.-W. Li, and J. von Delft, Controlled bond expansion for density matrix renormalization group ground state search at single-site costs, Phys. Rev. Lett. **130**, 246402 (2023).

[65] J.-W. Li, A. Gleis, and J. von Delft, Time-dependent variational principle with controlled bond expansion for matrix product states, Phys. Rev. Lett. **133**, 026401 (2024).

[66] A. Bohrdt, E. Demler, and F. Grusdt, Dichotomy of heavy and light pairs of holes in the t-J model, Nat. Commun. **14**, 8017 (2023).

[67] T. Guthardt, M. Scheb, J. von Delft, A. Bohrdt, and F. Grusdt, preceding paper, Magnetic polarons at finite temperature: One-hole spectroscopy study, Phys. Rev. B **112**, 205117 (2025).

[68] A. Weichselbaum, Non-Abelian symmetries in tensor networks: A quantum symmetry space approach, Ann. Phys. **327**, 2972 (2012).

[69] A. Weichselbaum, X-symbols for non-Abelian symmetries in tensor networks, Phys. Rev. Res. **2**, 023385 (2020).

[70] A. Weichselbaum, QSpace – an open source tensor library for Abelian and non-Abelian symmetries, SciPost Phys. Codebases 40 (2024).